

# Enhancing Predictability of Multi-Tenant DNN Inference for Autonomous Vehicles' Perception

Liangkai Liu\*, Kang G. Shin\*, Jinkyu Lee†, Chengmo Yang‡, and Weisong Shi‡

\*Department of Electrical Engineering and Computer Science, University of Michigan

†Department of Computer Science and Engineering, Yonsei University

‡Department of Computer and Information Sciences, University of Delaware

**Abstract**—Autonomous vehicles (AVs) rely on sensors and deep neural networks (DNNs) to perceive their surrounding environment and make maneuver decisions in real time. However, achieving real-time DNN inference in the AV's perception pipeline is challenging due to the large gap between the computation requirement and the AV's limited resources. Most, if not all, of existing studies focus on optimizing the DNN inference time to achieve faster perception, for example, by compressing the DNN model with pruning and quantization.

In contrast, we present a Predictable Perception system with DNNs (PP-DNN) that reduce the amount of image data to be processed while maintaining the same level of accuracy for multi-tenant DNNs by dynamically selecting 'critical' frames and regions of interest (ROIs). PP-DNN is based on our key insight that critical frames and ROIs for AVs vary with the AV's surrounding environment. However, it is challenging to identify and use critical frames and ROIs in multi-tenant DNNs for predictable inference. Given image-frame streams, PP-DNN leverages an ROI generator to identify critical frames and ROIs based on the similarities of consecutive frames and traffic scenarios. PP-DNN then leverages a FLOPs predictor to predict multiply-accumulate operations (MACs) from the dynamic critical frames and ROIs. The ROI scheduler coordinates the processing of critical frames and ROIs with multiple DNN models. Finally, we design a detection predictor for the perception of non-critical frames. We have implemented PP-DNN in an ROS-based AV pipeline and evaluated it with the BDD100K and the nuScenes dataset. PP-DNN is observed to significantly enhance perception predictability, increasing the number of fusion frames by up to 7.3×, reducing the fusion delay by >2.6× and fusion-delay variations by >2.3×, improving detection completeness by 75.4% and the cost-effectiveness by up to 98% over the baseline.

## I. INTRODUCTION

Deep neural networks (DNNs) have been widely used in the perception pipeline of autonomous vehicles (AVs) thanks to their high accuracy and ability to learn from raw data [1], [2]. For example, YOLOv3, SSD, and Faster R-CNN have been used for object detection [3]–[5]. Deeplabv3+ was proposed for semantic segmentation [6], [7], while LaneNet was designed for lane detection [8]. An AV's perception should be completed before a certain deadline with high accuracy [9]–[11].

Existing efforts focus on model compression to speed up the execution of DNN inference. Han *et al.* [12] proposed to prune redundant connections and re-train the deep learning models in order to fine-tune the weights effectively, thus reducing the computation requirement. Lowering the precision of operations and operands is another way of reducing the runtime of DNN inference [13]. However, it usually accompanies non-

negligible loss of accuracy, which is often unacceptable for AVs. Researchers also attempted to reduce the DNN inference time. DeepCache [14] leverages the temporal locality in streaming video to accelerate the execution of vision tasks on mobile devices. ALERT [15] used an anytime DNN system, which yields different outputs with different execution times. Liu *et al.* [16] proposed a self-cueing attention mechanism in critical regions for real-time object tracking. However, unlike general machine perception systems, the AV pipeline is usually equipped with multi-tenant DNNs running simultaneously, and hence their results need to be combined via fusion. Prophet [17] achieves timing predictability for multi-tenant DNNs *without* any accuracy guarantee. Guaranteeing the predictability of the AV perception is still a difficult and open problem.

Unlike the state-of-the-art (SOTA) studies that primarily focus on optimizing the DNN inference time to enhance accuracy, we seek a new and complementary opportunity: *Can we reduce the number of image frames to be processed without loss of accuracy by dynamically adjusting critical frames and regions of interest (ROIs)*? In AV perception, an image frame is said to be *critical* if it carries vital information that affects the AV's safety. A critical frame usually exhibits a noticeable difference from its preceding frames. We observe that the critical frames and ROIs for AVs vary with their surrounding environment. Given the temporal correlation within the continuous stream of images used for the detection of objects, processing every individual frame is not always necessary. The frequency of critical frames should instead be dynamically adapted to the specific driving and traffic conditions. Moreover, the configuration of ROI is also subject to environmental variations. For instance, when an AV stops at a traffic light, the ROI should cover all vehicles, pedestrians, bicycles, and other objects within its vicinity. On the other hand, the ROIs on a highway only need to cover the frontal and nearby vehicles.

We propose PP-DNN, an adaptive AV perception system, which dynamically selects critical frames and ROIs to guarantee predictability for multi-tenant DNN inference of objects in the AV's vicinity. For given image streams, PP-DNN first identifies critical frames and ROIs based on the similarity of consecutive frames in each image stream, box tracking, and traffic scenarios. It then coordinates the processing of critical frames and ROIs with multiple DNN models for environmental perception. As a result, PP-DNN not only reduces the computation requirement

but also achieves lower inference and fusion latencies without loss of perception accuracy.

Unfortunately, it is difficult to identify critical frames and ROIs for AVs while they are moving. For their adaptive and robust selection, PP-DNN proposes an ROI generator to choose representative frames with multi-level criteria. It first analyzes the pixel-level differences of consecutive frames using the *structural similarity* (SSIM) index. A lightweight tracker is designed to track stationary and moving objects to determine the ROIs together with the driving conditions like speed and highway or downtown. By combining the critical frame candidates with ROIs, the ROI generator dynamically produces and delivers critical frames to the inference pipeline equipped with multi-tenant DNNs.

It is difficult to process the selected critical frames with dynamic ROIs and multi-tenant DNNs because the variable ROI sizes cause the inference time to vary with the fusion of results from multiple DNN inference tasks, which may result in a longer delay or even failure of fusion. PP-DNN thus introduces a FLOPs predictor to predict Multiply-Accumulate Operations (MACs) for different ROIs. To reduce the fusion delay between multi-tenant DNNs, the frame scheduler monitors the delay for each task and determines the ROI for each task. Depending on the progress of fusion, it requests some tasks to yield resources or skip frames. Finally, PP-DNN introduces a detection predictor to generate anticipated results for non-critical frames, which decouples the detection from the fusion. The detection predictor takes the tracking results with selected ROIs to generate the velocity of bounding boxes for all moving objects. By combining it with the original image streams, PP-DNN predicts the coordinates of objects, lanes, and segmentation.

We have implemented PP-DNN in a Robot Operating System (ROS) based pipeline and evaluated it with real AV datasets: BDD100K and nuScenes [18], [19]. Overall, this paper makes the following four main contributions:

- Discovery of two unique characteristics (§III) for building a predictable perception pipeline via empirical studies.
- Design of the ROIs Generator (§IV-C) to model and detect ROIs in dynamic environments and development of the Detection Predictor (§IV-D) to predict detection results for non-critical frames using prior detections and temporal locality.
- Design of a Task Coordinator (§IV-E) to dynamically select ROIs, optimize input sizes for all perception tasks, and coordinate the execution order of critical frames and ROIs in multi-tenant DNNs.
- Addressing the lack of end-to-end testing by implementing PP-DNN atop ROS (§V) and evaluating it with real-world AV datasets (§VI), demonstrating that PP-DNN improves the number of fusion frames by up to  $7.3\times$ , reduces fusion delay by  $> 2.6\times$  and fusion-delay variations by  $> 2.3\times$ , improves detection completeness by 75.4% and cost-effectiveness by 98% over the baseline with general settings.

## II. BACKGROUND AND MOTIVATION

We first introduce DNNs in a general AV pipeline [1], [11] and then motivate the need for predictable perception .

### A. DNNs in AV Pipeline

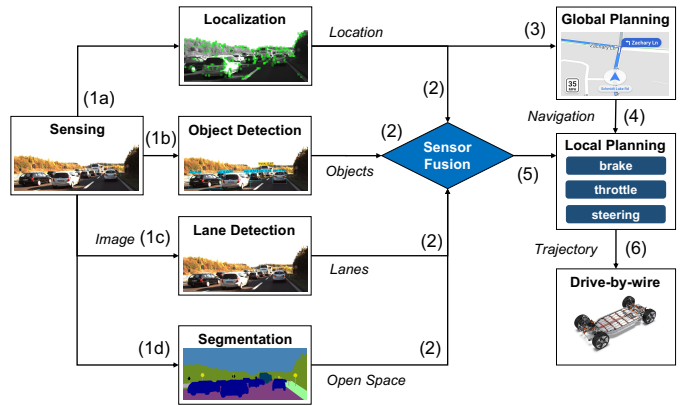


Fig. 1. A general autonomous driving pipeline.

Fig. 1 shows a generalized pipeline for modular AVs. A sensing node publishes the captured sensor data to all the perception nodes for localization (step 1a) [20], object detection (step 1b) [3], [5], [21], lane detection (step 1c) [8], [22]–[24], and segmentation (1d) [7], [25]. Next, the perception results are submitted to a sensor fusion node (step 2), which combines the information on the vehicle’s location, objects, lanes, and open spaces [2], [26]. The location is also published to the global planning node to calculate a navigation route to the destination [27]. The navigation route (step 4) and sensor fusion results (step 5) are both published to the local planning stage [28], which constructs a local driving space cost map and generates and publishes vehicle trajectories to the vehicle’s drive-by-wire system (step 6) [29], [30]. Finally, the drive-by-wire system will send control messages to Electronic Control Units (ECUs) through the Controller Area Network (CAN) to maneuver the vehicle [31].

Within the processing pipeline, the multi-tenant DNN inference serves as a foundation of the AV perception system. Multi-tenant DNN tasks run concurrently, merging their outputs based on timestamps to provide real-time updates on nearby moving objects, drivable areas, traffic lights/signs, etc. [1].

### B. Motivation for Predictable Perception

The safety of AVs hinges on real-time and accurate perception of their environment, necessitating predictability in both temporal and functional aspects [9]. Temporal predictability ensures the perception process is completed within a anticipated time frame, allowing other modules to respond appropriately. Functional predictability requires the perception module to provide accurate and comprehensive coverage of the dynamic traffic environment.

We address these challenges by proposing a novel approach that *reduces the number of image frames processed to improve*

timing performance without sacrificing accuracy. By dynamically adjusting critical frames and ROIs using temporal locality, we improve timing and functional predictability.

### III. EMPIRICAL STUDIES

This section provides some of the insights gained from our empirical studies of temporal locality and inference-time variations in the AV's perception.

#### A. Revisiting Temporal Locality

Although a camera usually produces frames at 30 FPS, it is not necessary to process all of them owing to the high similarities between the consecutive frames. The SOTA approaches focus on leveraging the locality of pixels for real-time DNN inference [14], [32]. However, these similarity-based approaches ignore environmental information, thus limiting their capability.

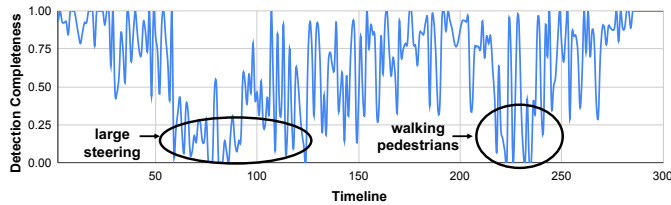


Fig. 2. The timing analysis of the detection completeness ratio for each frame when FPS = 5.

**Environment-aware critical frames.** We argue that the selection of critical frames should be scenario-aware, i.e., the number of critical frames should vary with the underlying traffic scenario. Fig. 2 provides a timing analysis for the detection completeness relative to a 30 FPS speed when the FPS is reduced to 5. Detection completeness is calculated as the percentage of objects being detected from selected critical frames relative to the case of processing all frames. From the timeline, we can observe two periods of low detection completeness. With some driving context information from the image stream, we found the large steering control during the first period caused higher pixel changes in consecutive frames. Nearby walking pedestrians caused low detection completeness during the second period. The movement of pedestrians makes the intersection over union (IoU) lower than 0.5 in the original image. In both cases, it could cause safety problems if the detection misses occur. Therefore, critical frames must be selected in an environmental-aware manner.

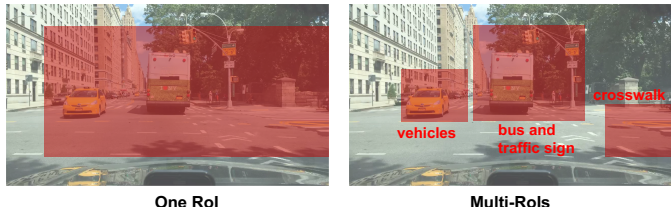


Fig. 3. An example of environment-aware dynamic ROIs.

**Environment-aware dynamic ROIs.** We argue the ROI must also be environment-aware for both critical and non-critical

frames [33]. An ROI describes the critical region that must be detected both timely and accurately. The SOTA approaches mainly consider one ROI on a single frame, usually requiring the ROI to cover all the areas of interest. In contrast, we found that multiple ROIs can be more efficient than a single ROI in terms of reducing input size. Fig. 3 shows an example of one and multiple ROIs in a single frame. One can observe that the ego vehicle needs to track the vehicle on the left, the bus in front, traffic lights and signs, and pedestrians crosswalk on the right. The left image shows the use of one big ROI to cover all these areas, while the right image uses three ROIs to cover the vehicle, the bus and traffic sign, and the crosswalk. Both ensure comprehensive coverage of essential areas.

**Insight 1:** *Critical frames and ROIs vary with the environment and needs to be determined dynamically. Using multiple ROIs can reduce the size of critical input more effectively than a single ROI.*

#### B. Revisiting Inference Time Variations

The use of dynamic critical frames and ROIs reduces the size of input to the DNN inference, but also increases the inference-time variation. The trained DNN models with two-stage-based structures are shown to have higher inference-time variations than one-stage-based structures [17], [32], [34]. Note, however, that we focus on the inference-time variations caused by variable ROI size and multi-tenant DNNs.

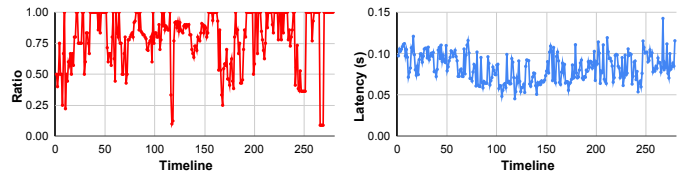


Fig. 4. The area ratio for consecutive frames and the corresponding inference time using Faster R-CNN.

**Image size and time variations.** In general, the ROI needs to cover all the critical objects, so we define ROI as the minimum cover of all the detected objects in each frame. By applying this definition to the BDD100K dataset, we calculate the ratio of ROI area to the original image size. Fig. 4 shows the timeline of the ratio and the inference latency when the cropped images are applied to the Faster R-CNN model. One can observe that the ratio changes dynamically and is mostly less than 1, making it unnecessary to process the entire frame. Moreover, dynamic ROIs contribute to the inference-time variations of the Faster R-CNN model.

To better understand the relationship between image size and inference-time variations, we generated different image sizes: width ranging from 10 to 720 and height ranging from 10 to 1280, both with a step size of 10. By applying these images of different sizes to the model for inference, we collect the Multiply-accumulate operations (MACs) which dominate the inference time. Four DNN models—Faster R-CNN [5], SSD [4], Deeplabv3 [35], LaneNet [8]—in AV perception are tested with variable input-image sizes. Both Deeplabv3 and LaneNet show a normal trend of large image sizes having

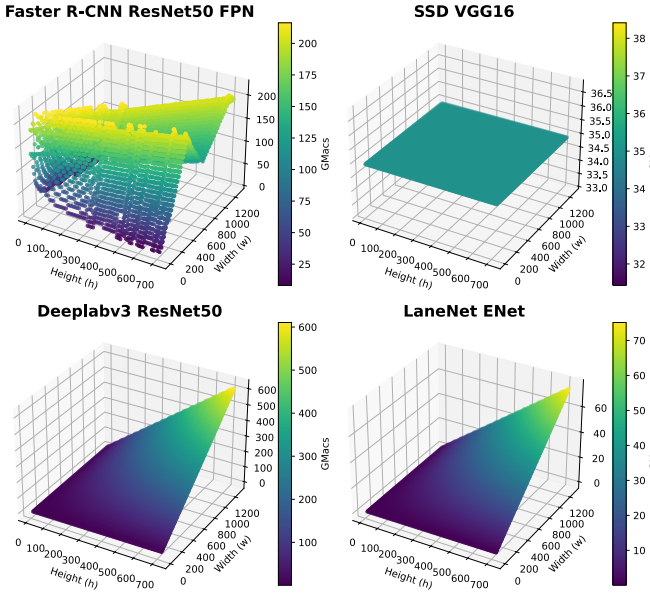


Fig. 5. GMACs of different image sizes (Height, Width) for DNN models in the perception.

higher Giga Multiply-Add Operations (GMACs). Fig. 5 shows the scatter plot of GMACs for Faster R-CNN and SSD. We can observe that Faster R-CNN shows a special GMACs peak with some small images while SSD shows static GMACs for all image sizes. We find the root cause of this difference from layer-wise GMACs and input/output sizes, i.e., pre-processing images causes this difference. All two-stage-based models, like Faster R-CNN, are designed to take variable size inputs and the images go through variable ranges [5]. This resizing makes some small images have large MACs. One-stage model like SSD takes static input so all the images are resized to a fixed size. In contrast, segmentation models like Deeplabv3 and LaneNet do not resize the images. To determine the ROIs with minimum MACs, the resizing during the pre-processing of DNN models needs to be accounted for.

**Unpredictability of Multi-tenant DNNs Inference Time.** To understand the inference-time variations in multi-tenant DNNs, three DNN models are deployed onto three GPU cards (Faster R-CNN, DNLNet, and Deeplabv3+), and `message_filter` in an ROS is leveraged to merge results in a time window [36], [37]. A group of over 4800 images from the BDD100K dataset are published as the ROS image streams at 30 FPS. Each image is assigned a unique sequence number, starting from 0. To process these images, three DNN tasks are initialized, waiting for ROS image data. These tasks are triggered by callback functions — where a function is passed as an argument into another function — to be invoked or executed within the outer function. This ensures the tasks respond immediately to incoming images for processing. Fig. 6 shows the result for the inference delay of each task and fusion delay. It also includes the cumulative distribution function (CDF) of frame sequence number difference when entering callback functions. The frame sequence number difference reflects the queuing delay of the

frame entering the callback function. We can observe that the fusion delay is much higher than the combination of the inference-time variation for each single DNN. The fusion delay increases because the ROS subscriber uses multiple threads to handle incoming ROS images. Consequently, some threads process outdated frames from the message queue. This observation is corroborated by the CDF of the frame sequence number difference, where a notable portion of delay falls within the 10–15. Given the execution on GPU is not preemptable [38], the coordination of multi-tenant DNNs should be ROIs-aware.

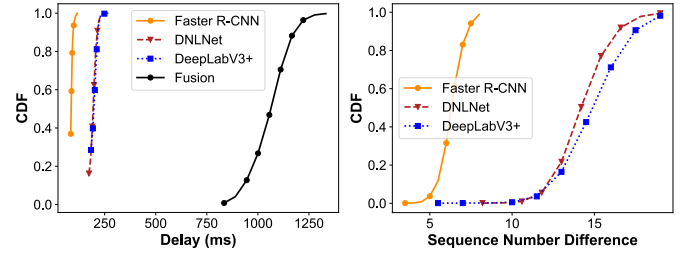


Fig. 6. The CDF of DNN inference delay, fusion delay, and sequence number difference

**Insight 2:** *Dynamic input size and out-of-date frames are the root cause of inference-time variations in the AV's perception. There is a non-linear relationship between input size and GMACs for DNN models. Coordination of multi-tenant DNNs inference should be ROI-aware.*

#### IV. SYSTEM DESIGN

We present the design of PP-DNN, including an ROI generator to select critical frames with dynamic ROIs for the AV's perception, a predictor to cache and predict the detection of objects, and a coordinator to determine/identify critical frames and ROIs for each DNN inference task.

##### A. Overview

Fig. 7 provides an overview of PP-DNN. PP-DNN supports the predictability of the AV's perception with three functional components/modules. First, the ROIs generator determines/identifies critical frames from the image stream by leveraging the pixel-level SSIM index and box-level tracking results. Depending on the location of detected objects and their environmental context, the generator produces a set of ROIs for each task. This set encompasses both single and multiple ROIs. Second, the selected critical frames and their associated ROIs are forwarded to the task coordinator. The expected FLOPs for each ROI are estimated using the FLOPs predictor. The frame scheduler then selects the ultimate critical frames and their respective ROIs for each task, prioritizing those with the lowest FLOPs. Third, the detection predictor publishes the detection results for non-critical frames to the fusion node. This predictor comprises both a box predictor and a segmentation predictor. The former retains all the tracking and detected bounding boxes associated with critical frames. Meanwhile, the segmentation predictor, informed by the ROIs and the box predictor's outputs, forecasts the current state of

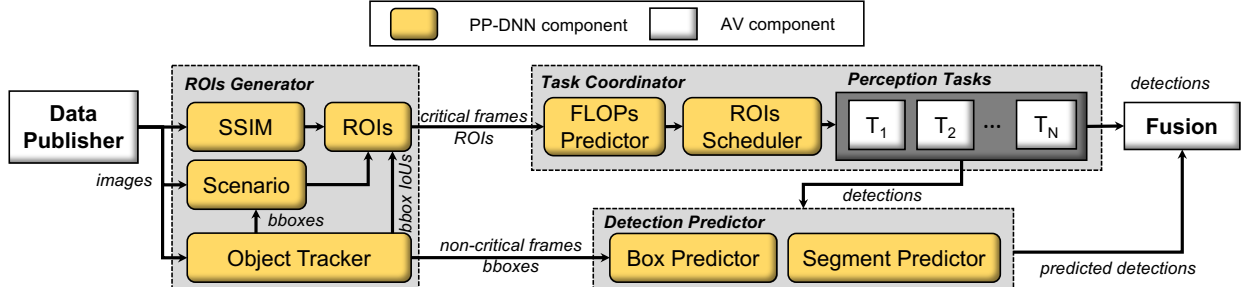


Fig. 7. An overview of PP-DNN.

semantic segmentation. These predictions are updated at the image stream's frame rate, ensuring detection results at a high frequency. These results are then published as ROS messages.

### B. Technical Challenges and Contributions

To support a predictable perception pipeline, PP-DNN addresses the following challenges:

#### C1: How to model and detect ROIs in dynamic environments?

The ROIs are expected to provide minimum coverage of all the areas critical to AV safety. The ROIs should also be adapted to the dynamic environments. The pixel-wise similarity is commonly used to filter critical frames. In PP-DNN, we check the pixel- and bounding-box-level similarity and the traffic scenario in real time.

#### C2: How to choose ROIs to reduce inference-time variations?

Dynamically changing input size causes the DNN inference time to vary. PP-DNN uses the relationship between MACs and image size to determine ROIs for all perception tasks.

#### C3: How to predict the detection results for non-critical frames?

Compared to running inference on critical frames with ROIs, the detection results for non-critical frames are predicted based on previous critical-frame detection and temporal locality.

#### C4: How to coordinate multi-tenant DNNs inference to reduce fusion-time variations?

In PP-DNN, the coordinator determines the ROIs and the critical frame execution order to reduce the fusion delay.

### C. ROIs Generator

To guarantee functional predictability, the choice of ROIs should be environment-aware and provide complete coverage of the moving objects and traffic segments. The ROIs generator produces critical frames of ROIs based on the pixel-level SSIM, bounding boxes tracking, and traffic scenarios.

**Pixel-level SSIM.** SSIM reflects the structural similarity of pixels of images. To ensure the SSIM index is sensitive to object-level pixel changes, we first resize the image to a  $25 \times 25$  greyscale image using a high-quality Lanczos filter [39]. The SSIM is calculated based on [40]. A sliding window of size  $11 \times 11$  with step size 1 is used to get patches from both images. For each patch, the SSIM is calculated using Eq. (1), while the final SSIM of the image is the average SSIM of all the patches. When calculating the mean and variance of each patch, a Gaussian convolution kernel with a variance of 1.5 is used as

a weighted average [40]. If the SSIM with the previous frame is less than a threshold, the current frame will be critical.

$$\text{SSIM}(x, y) = \frac{(2\mu_x\mu_y + c_1)(2\sigma_{xy} + c_2)}{(\mu_x^2 + \mu_y^2 + c_1)(\sigma_x^2 + \sigma_y^2 + c_2)} \quad (1)$$

**Bounding boxes IOU.** Bounding box-level IOU reflects the locality of the detection results. We implement a light-weight object tracker based on DeepSort with YOLOv4-tiny to predict and update the ID and bounding boxes of moving objects for each frame [41]–[43]. Given the pixel- and box-level temporal locality for high FPS consecutive frames, the tracking can be accurate for most of the time [32]. The output of the tracker includes all missed, tracked, and detected objects. For all tracked objects, bounding box IOU is calculated to show the box-level similarity of two consecutive frames. If either the number of missed objects or the average bounding box IOU for tracked objects is less than a preset threshold, the current frame will be critical.

**IOUs.** After tracking, a bounding box will be generated for each tracked object. Suppose  $n$  is the sequence number of the current frame and  $M$  is a set that contains all the tracked objects. Based on the tracking objects, we can generate two types of ROIs for each task from the ROIs generator: one or multiple ROIs. Fig. 3 shows an example for both one and multiple ROIs choices. Multi-ROIs contain all the objects' bounding boxes together according to Eq. (2), while a single ROI uses one rectangular box to cover all the tracked bounding boxes. Eq. (3) shows how to calculate by finding the top left corner with the width and the height.

$$\text{Multi-ROIs: } = \{x_j^{(n)}, y_j^{(n)}, h_j^{(n)}, w_j^{(n)}\}, \forall j \in M \quad (2)$$

$$\text{One-ROI: } = \{\min_{\forall j \in M} x_j^{(n)}, \min_{\forall j \in M} y_j^{(n)}, \max_{\forall j \in M} h_j^{(n)}, \max_{\forall j \in M} w_j^{(n)}\} \quad (3)$$

**Scenario & time interval awareness.** Another critical factor that could impact AV safety is the traffic scenario. Based on the detection results for objects, the traffic scenario is determined based on the percentage and class of moving objects and stationary objects. The target moving objects include all types of vehicles (cars, buses, trucks, motorcycles, etc.), pedestrians, and bicycles. Stationary objects include traffic signs and traffic

lights. The ratio of each class will be calculated and monitored. If the stationary object ratio is close to 0, the choice of ROIs will be more focused on dynamic objects' bounding boxes. Otherwise, a dedicated ROI will be assigned to keep track of traffic lights/signs. For moving objects, if the pedestrians' ratio is  $> 0.5$ , a ROI with complete object coverage will be used.

The time interval is another factor for critical frame selection. Although there is a minor difference between consecutive frames, the accumulation of slight differences could be large. Therefore, we monitor the time interval between critical frames and set a timer with the deadline. If the time interval between the current time and the last critical frame exceeds the deadline, the current frame will be a critical one.

#### Algorithm 1 Critical Frame Selection Process

```

1: Input: Current frame  $F_{current}$ , Previous frame  $F_{previous}$ , Critical frame interval  $T_{interval}$ , Traffic scenarios  $S_{traffic}$ , SSIM threshold  $\tau_{SSIM} = 0.95$ 
2: Output: Set of critical frames  $C$ 
3:  $C \leftarrow \emptyset$  ▷ Initialize the set of critical frames
4: for each frame  $F_{current}$  do
5:   if  $T_{interval} > deadline$  or  $F_{current} \in S_{traffic}$  then
6:      $C \leftarrow C \cup \{F_{current}\}$  ▷ Mark frame as critical
7:   else
8:      $SSIM \leftarrow SSIM(F_{current}, F_{previous})$ 
9:     if  $SSIM < \tau_{SSIM}$  then
10:       $C \leftarrow C \cup \{F_{current}\}$  ▷ Mark frame as critical
11:    else
12:       $bbox\_pred, obj\_miss \leftarrow \text{Tracker}(F_{current})$ 
13:      if  $obj\_miss > 1$  then
14:         $C \leftarrow C \cup \{F_{current}\}$  ▷ Mark frame as critical
15:      end if
16:    end if
17:  end if
18:  if  $F_{current} \in C$  then
19:    Generate one-ROI / multi-ROIs
20:  end if
21: end for
22: return  $C$ 

```

#### D. Detection Predictor

In PP-DNN, a detection predictor is designed to temporally predict the bounding boxes and semantics for updating the detection results with high FPS. The predictor includes two parts: (i) box predictor, which predicts bounding boxes based on tracking results, and (ii) a segmentation predictor, which predicts the segmentation's current status and published as ROS messages.

**Box predictor.** Based on the analysis of the fusion of multi-tenant DNN inference, the "wooden barrel effect" slows down the fusion process. The detection process is the DNN inference which is time-consuming while the fusion node waits for the results for message synchronization. Therefore, PP-DNN addresses this challenge by decoupling the detection process with the results publishing process. Here we store separate detection queues for three tasks. For object detection, bounding boxes, scores, and timestamps are saved. For semantic segmentation and lane detection, segmentation images with pixels marked as segmentation labels are saved. The queue

length is maintained to include 10 critical frame detections in the queue. The history of results will be deleted when new critical frames are added to the queue. The object detection prediction is mainly based on the tracker's output. For each tracked object, we calculate the maximum IoUs with the cached object detection results. If IoU is larger than 0.5, the bounding box will be updated with the tracking results. If the IoU is less than 0.1, the cached bounding box will be kept while another bounding box is based on the tracker. The cached bounding box will be updated when a new critical frame completes the inference.

**Segmentation predictor.** The segmentation predictor is responsive to predict the updated pixel semantics. Since both lane detection and semantic segmentation are updating segmentation images, we propose a velocity-based prediction for updating segmentation pixels. Fig. 8 shows the design of the segmentation predictor.

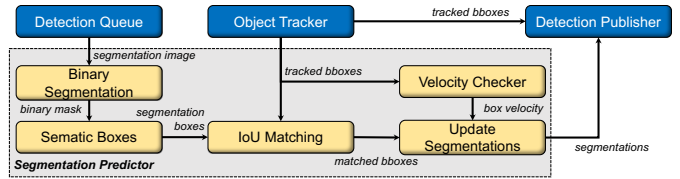


Fig. 8. The design of the segmentation predictor in the predictor module.

For segmentation images cached by the detection queue, the segmentation predictor first converts it to a binary segmentation image where segmentation will be one while the background will be 0. Next, segmentation bounding box coordinates will be extracted from the binary segmentation mask. Meanwhile, the tracker's output with tracked bounding boxes for objects is read, calculating the IOU with the segmentation bounding boxes. The two boxes are matched similarly if the IOU is larger than 0.5. The tracker also calculates the velocity, which includes the difference in the x-axis, y-axis, height, and width using the tracked bounding boxes' movement. Eq. (4) shows the calculation of box velocity based on the coordinates of tracked boxes in continuous frames. For all matched boxes, the velocity is applied to update the segmentation pixels. Finally, the updated segmentation results will be sent to the detection publisher. For lane detection, we use the last critical frame's output as the updated lanes since we observe limited differences from the detection results of consecutive frames.

$$V_{box} = (x_{min}^{(n)} - x_{min}^{(n-1)}, y_{min}^{(n)} - y_{min}^{(n-1)}, h^{(n)} - h^{(n-1)}, w^{(n)} - w^{(n-1)}) \quad (4)$$

#### E. Task Coordinator

In PP-DNN, the task coordinator is designed to determine the critical frame and ROIs to reduce the fusion delay.

**FLOPs predictor.** With the understanding of the impact of image sizes on MACs for perception models in Section III, we formulate a model for predicting the total FLOPs for the perception pipeline. Eqs. (5), (6), and (7) show the FLOPs of object detection, lane detection, and segmentation for one

given ROI box. We can observe that the FLOPs for the object detection model is segmented function with respect to the height/width ratio. This is mainly because the object detection model has a pre-processing stage that resizes the image into a range of size  $[s_{min}, s_{max}]$ . Besides, the ceiling is applied to the resized image to make all sizes divisible by  $s_d$ . The size range is [800, 1333] while the divisible size is 32. For segmentation tasks, since there is no resizing, the FLOPs are calculated directly.

$$f_0(h, w) = \begin{cases} a_0 \left[ \frac{s_{max}h}{w \cdot s_d} \right] \cdot \left[ \frac{s_{max}}{s_d} \right] \cdot s_d^2 & 0 < \frac{h}{w} \leq \frac{s_{min}}{s_{max}} \\ a_0 \left[ \frac{s_{min}}{s_d} \right] \cdot \left[ \frac{s_{min}w}{h \cdot s_d} \right] \cdot s_d^2 & \frac{s_{min}}{s_{max}} \leq \frac{h}{w} \leq 1 \\ a_0 \left[ \frac{s_{min}h}{w \cdot s_d} \right] \cdot \left[ \frac{s_{min}}{s_d} \right] \cdot s_d^2 & 1 \leq \frac{h}{w} \leq \frac{s_{max}}{s_{min}} \\ a_0 \left[ \frac{s_{max}}{s_d} \right] \cdot \left[ \frac{s_{max}w}{h \cdot s_d} \right] \cdot s_d^2 & \frac{s_{max}}{s_{min}} \leq \frac{h}{w} \end{cases} \quad (5)$$

$$f_1(h, w) = a_1 hw \quad (6)$$

$$f_2(h, w) = a_2 hw \quad (7)$$

**ROIs scheduler.** Since different tasks could have different critical frames and ROIs, the ROI scheduler takes the FLOPs prediction results for each task and chooses  $(h, w)$  to minimize the FLOPs for each frame. Multi-ROIs are packed as one batch for DNN inference, while ML libraries like Pytorch require all images in one batch to have the same size. Therefore, we apply the largest size in multi-ROIs to extract multi-ROIs before FLOPs prediction. The ROIs scheduler determines the choice of one-ROI or multi-ROIs based on the predicted FLOPs.

In the perception pipeline in Fig. 1, each task—detection, segmentation, and fusion—subscribes to the camera stream and fires its callback as soon as a new frame arrives. A lightweight, distributed scheduler maintains a shared state that records the latest sequence numbers and deadlines, and dispatches critical frames according to three rules. First, if a task has already missed its per-frame deadline, the incoming frame is routed exclusively to that task. Second, if the traffic-scenario detector flags the frame as safety-critical (e.g., cut-in vehicle, pedestrian crossing), it is broadcast to all tasks. Third, for all other frames, the scheduler computes each task’s delay—the sequence-number gap between the candidate frame and the task’s most recent output—and drops the frame for any task whose delay exceeds a task-specific threshold. This threshold is derived from the static end-to-end deadline and the camera frame rate (e.g., six frames for a 200 ms budget at 30 FPS). Together with a prediction module that refreshes single-task outputs at the camera’s frame rate, this dispatcher bounds per-task latency and ensures timely multi-task fusion, enabling PP-DNN to meet the hard real-time requirement of autonomous driving.

## V. IMPLEMENTATION

To fill the gap for end-to-end perception testing and evaluation, we integrate the implementation of PP-DNN into an AV perception pipeline based on ROS in a GPU platform.

**ROS framework.** Based on the AV system in Fig. 1, we develop a ROS framework for its perception system, as shown in Fig. 9. The ROS framework focuses on the DNN-based perception tasks. The pipeline starts with the */image* node, capturing and publishing images from the cameras. Three ROS nodes subscribe */image\_raw* messages and execute the DNN inference on the images, including object detection, lane detection, and semantic segmentation. The *ROIs generator* node subscribes to the */image\_raw* topic, determines critical frames and ROIs, and sends to the *ROIs dispatcher* node. The tracker and the predictor subscribe to the results from the three DNN tasks and publish predicted results to the */fusion* node.

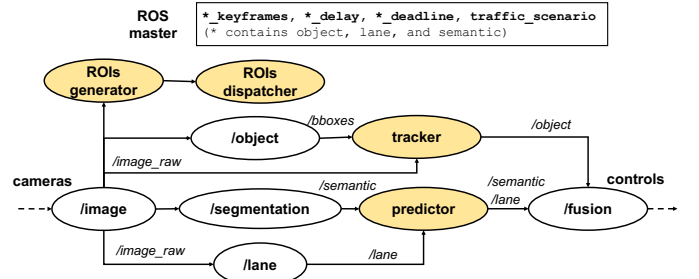


Fig. 9. The ROS implementation of the PP-DNN system.

Moreover, the critical frames on each task are dispatched based on the ROS parameters which are global variables managed by the ROS master. We define 10 ROS parameters for passing three tasks’ critical frame sequence ID, delay, deadline, and traffic scenario.

**Message synchronization.** In ROS, message synchronization is achieved by using the timestamp and sequence number/ID. The */fusion* node combines all the perception results of the same image frame. First, we have to generate a unique ID for each image frame. In the beginning, the */image* node attaches a timestamp and frame ID to each message it publishes. The timestamp and sequence ID of the incoming images will be used as the header’s timestamp and sequence number of the new message like */object*, */semantic*, etc. With unique IDs on each image frame and detection results, we implement a *message\_filter* with the Approximate Time Synchronizer to manage the fusion process [37]. The approximate synchronizer sets queue size as 1000 and 300ms as the slop, which means the message with a time difference of less than 300ms is considered synchronized.

**Detection completeness.** To show how good the selected critical frame’s performance is in environmental perception, based on the Pseudo ground truth concept in [32], we propose a detection completeness metric that calculates the number of detected objects in critical frames compared to the baseline, which processes all the frames. An object is detected if the detected bounding box has over 0.5 IoU with the baseline’s detection results. The pseudo-code for detection completeness calculation is shown in Algorithm 2. The input contains the detection results for a group of frames for the keyframes and the baseline (process all the frames). First, identify the frame index *index\_key* in the keyframes’ results (Lines 3-5). Second,

go through all the bounding boxes in that frame and calculate the max IoU with the keyframe's detection results (Lines 6-7). For each object, if the score is larger than 0.5, the number of objects will be increased by 1. If the max IoU is larger than 0.5 and the detected score in the keyframe is larger than 0.5, then the detected object is increased by 1. After checking all the frames, the detection completeness  $d_c$  is calculated using *detected* divided by *objects*.

### Algorithm 2 Detection Completeness

```

1: Input: Keyframes' bounding boxes  $D_k$ , scores  $S_k$ , timestamps  $t_k$ ; Offline detections' bounding boxes  $D_a$ , scores  $S_a$ , timestamps  $t_a$ 
2: Output: Detection completeness  $d_c$ 
3:  $detected \leftarrow 0$ ,  $objects \leftarrow 0$ 
4:  $index\_key \leftarrow 0$ 
5: for  $index$ ,  $frame$  in  $D_a$  do
6:   if  $t_a[index] > t_k[index\_key]$  then
7:      $index\_key \leftarrow index\_key + 1$ 
8:   end if
9:   for  $box\_id$ ,  $boxes$  in  $frame$  do
10:     $mIoU$ ,  $nmax \leftarrow \text{maxIoU}(D_k[index\_key], boxes)$ 
11:    if  $S_a[index][box\_id] > 0.5$  then
12:       $objects \leftarrow objects + 1$ 
13:      if  $mIoU > 0.5$  and  $S_k[index\_key][nmax] > 0.5$ 
        then
14:           $detected \leftarrow detected + 1$ 
15:        end if
16:      end if
17:    end for
18:  end for
19:   $d_c \leftarrow detected/objects$ 
20: return  $d_c$ 

```

## VI. EVALUATION

We evaluate the effectiveness of PP-DNN in guaranteeing the predictability of AV perception through comprehensive experiments with an ablation study. Our key findings are:

- PP-DNN significantly improves multi-tenant DNN inference. The detection predictor helps increase the number of fused frames by up to  $7.3\times$ . The frame dispatcher helps shorten the fusion delay by  $>2.6\times$  and fusion delay variations by  $>2.3\times$ . PP-DNN guarantees the timing predictability of the perception pipeline. (§VI-B).
- The detection completeness effectively captures the streaming detection performance. PP-DNN improves the completeness of object detection by 75.4%. It guarantees the functional predictability for the perception pipeline. (§VI-C).
- PP-DNN significantly improves latency and accuracy, making up to a 98% improvement in cost-effectiveness. (§VI-D) while incurring (acceptable) 20% CPU and 39.3% GPU memory-consumption overheads.

### A. Experimental Setup

We first present the setup used for the implementation and evaluation of PP-DNN. We choose a GPU platform as the computing device following general AV settings [44], [45] and use the BDD100K dataset and the nuScenes mini dataset as

TABLE I  
THE NAMES AND CONFIGURATIONS OF FIVE TESTING CASES.

Testing Cases Name	Configurations
Baseline	Base
FD	Base + Dispatcher
FD+FG	Base + Dispatcher + ROI
FD+DP	Base + Dispatcher + Predictor
PP-DNN	Base + Dispatcher + ROI + Predictor

the input to the perception pipeline [18], [19]. The BDD100K dataset is composed of 2,629 image frames covering 12 traffic scenarios at 30 FPS. The nuScenes dataset includes 1,938 images covering 10 traffic scenarios at 12 FPS. These images are published as ROS Image.

**Hardware and software setup.** The GPU platform has 8 Intel® Core™ i9-9940X CPUs with the highest frequency of 3.3GHz and 32 GB DDR4 CPU memory. The platform has one NVIDIA A10G Tensor Core GPU cards with 24GB GDDR6 GPU memory [45]. It provides 31.2 teraFLOPS for FP32. The libraries installed for ML-related applications include CUDA Driver 510.47.03, CUDA runtime 11.6, TensorFlow 1.15.2, torch v1.10.1, torchvision v0.11.2, cuDNN 8.3.2, OpenCV 4.2, etc. ROS Melodic is deployed as the communication middleware. Since it is essential to meet the required accuracy for AVs, all the DNN models are those trained from the BDD100K model zoo, and tested with full precision (FP32) [18]. Faster R-CNN, DNLNet, and Deeplabv3+ are deployed for object detection, lane detection, and semantic segmentation [5], [35], [46]. Approximate Time Synchronizer in ROS *message\_filter* is deployed for sensor fusion [36], [37].

**Testing Cases.** We consider five testing cases to evaluate the impact of PP-DNN's modules on the fusion delay and detection completeness. FD follows the same design for multi-tenant DNNs coordination as Prophet [17]. Table I shows the names and configurations of these five testing cases. In the base configuration, all the frames are published and processed in the ROS data stream system. We conduct ablation experiments on the impact of the frame dispatcher (FD), the critical frame ROI generator (FG), the detection predictor (DP), and PP-DNN.

**Metrics.** We primarily focus on three metrics: latency, accuracy, and cost-effectiveness. In terms of latency, we evaluate both the single DNN inference time and the overall end-to-end fusion delay, in addition to comparing the number of processed frames. For accuracy, we employ detection completeness to assess the performance of detecting all cases against the offline ground truth. Lastly, we examine the cost-effectiveness across all cases which is defined as the average fusion latency divided by fusion accuracy; This is the fusion ratio times the average detection completeness of multiple perception DNN models.

$$\text{Cost-effectiveness} = \frac{\text{average latency}}{\text{fusion percent} \times \text{average accuracy}}. \quad (8)$$

This cost-effectiveness ratio highlights the PP-DNN's efficiency in enhancing both latency and accuracy.

### B. Multi-Tenant DNN Inference Fusion

Since PP-DNN is designed to make the perception pipeline predictable, the multi-tenant DNN inference fusion performance becomes our primary goal. Below we discuss the fusion performance in terms of the number of fusion frames, the fusion delay, and the worst-case fusion delay.

**Fusion Frames.** The number of fusion messages reflect the system's ability to process high FPS sensor data. We use two datasets: the BDD100K dataset containing 2,629 images and the nuScenes mini v1.0 dataset with 1,938 images as the workload of the perception pipeline and collect the number of fusion and processed frames for all the testing cases. The results are presented in Tables II and III, showing that the baseline's fusion frames over all the frames (2,629) is just 8.6%. The introduction of the frame dispatcher and critical frame selector does not make PP-DNN process more frames than the baseline, because PP-DNN is designed to trade the number of processed frames for better fusion performance. The comparison of different test cases shows that introducing the detection predictor (DP) greatly increases the number of fusion messages because the DP publishes prediction detection messages to the fusion when the detection process is not updated. This decoupling allows the prediction to run in parallel with the detection, making more messages fused. Table II shows PP-DNN to achieve 62.5% fusion frames compared to the baseline's 8.6%, making nearly a  $7.3\times$  improvement. Table III presents the result on the nuScenes dataset, showing PP-DNN's achievement of 48% fusion frames compared to the baseline's 20.8%, which is a  $2.3\times$  improvement. The main difference between BDD100K and nuScenes datasets is the FPS. At a lower FPS (12Hz), the similarities between consecutive frames are lower for the nuScenes dataset. However, PP-DNN still makes a large improvement in the number of fusion frames, indicating the effectiveness of the detection predictor.

TABLE II  
THE NUMBER OF PROCESSED FRAMES ON BDD100K.

Frames	Faster R-CNN	DNLNet	Deeplabv3+	Fusion	Percent (%)
Baseline	335	286	227	227	8.6
FD	332	282	227	212	8.1
FD+FG	444	491	303	264	10.0
FD+DP	367	322	257	<b>1925</b>	<b>73.2</b>
PP-DNN	<b>459</b>	<b>536</b>	<b>322</b>	1642	62.5

TABLE III  
THE NUMBER OF PROCESSED FRAMES ON NUSCENES.

Frames	Faster R-CNN	DNLNet	Deeplabv3+	Fusion	Percent (%)
Baseline	612	517	410	403	20.8
FD	609	514	410	376	19.4
FD+FG	679	518	446	412	21.3
FD+DP	604	761	412	<b>964</b>	<b>49.7</b>
PP-DNN	<b>661</b>	<b>824</b>	<b>445</b>	930	48.0

**Fusion Delay.** Another essential metric for the AV's safety

is the end-to-end delay for the fusion process, defined as the time from capturing the image to finish the fusion. We collect the fusion delay, inference delay, and image sequence number difference for all test cases. The results of the fusion delay are shown in Fig. 11. From Fig. 11, we can observe that PP-DNN makes a significant improvement in the fusion delay over the baseline. Table V shows the average delay for all test cases on the BDD100K dataset. PP-DNN speeds up the fusion by  $5.7\times$  (from 1988.8ms to 349.1ms). Table VI shows the result on the nuScenes dataset, showing PP-DNN's speedup of the fusion by  $2.6\times$  (from 1627.6ms to 632ms). By comparing the baseline with FD, we can find that the frame dispatcher helps reduce the fusion delay by coordinating multi-tenant DNN inference. Besides, from the comparison of FD with FD+FG, we can observe that introducing the critical frame ROI generator reduces the latency.

Table IV shows the fusion-delay variations on both datasets. PP-DNN significantly reduces the variations, primarily thanks to the frame dispatcher, which skips out-of-date frames, thereby reducing the maximum delay. The detection predictor also contributes by predicting results, which reduces both the minimum and maximum fusion delays. We find that PP-DNN narrows the range to 607 ms on the BDD100K dataset, which is approximately  $2.7\times$  narrower than the baseline range of 1640 ms. Similarly, for the nuScenes dataset, PP-DNN decreases the range to 582 ms, which is about  $2.3\times$  narrower than the baseline range of 1315 ms.

TABLE IV  
FUSION-DELAY VARIATIONS.

Fusion Delay Variations (ms)	BDD100K			nuScenes		
	min	max	range	min	max	range
Baseline	432	2072	1640	417	1732	1315
FD	363	797	<b>434</b>	403	908	505
FD+FG	380	857	477	475	1069	594
FD+DP	<b>54</b>	<b>538</b>	484	412	<b>834</b>	<b>422</b>
PP-DNN	59	666	607	<b>301</b>	883	582

**Worst-Case Analysis.** Besides the average delay, our comparison of worst-case performance of the baseline and PP-DNN takes into account the 99-th percentile of fusion latency, as depicted in Fig. 10. On the BDD100K dataset, we observe a substantial reduction of the worst-case fusion delay with PP-DNN, from 815ms to 505ms, a decrease of 38%, as opposed to the baseline's delay of  $>800$ ms. For the nuscenes dataset, PP-DNN reduces the worst-case fusion latency by 17.5%, from 664ms to 548ms. Ablation studies indicate the frame dispatcher (FD) helps make these improvements by orchestrating multi-tenant DNN inference execution and skipping outdated frames. Moreover, the introduction of the frame ROI generator (FG) and detection predictor (DP) incurs some latency overhead. Nonetheless, PP-DNN manages to achieve a balanced fusion delay, effectively improving worst-case fusion latency over the baseline.

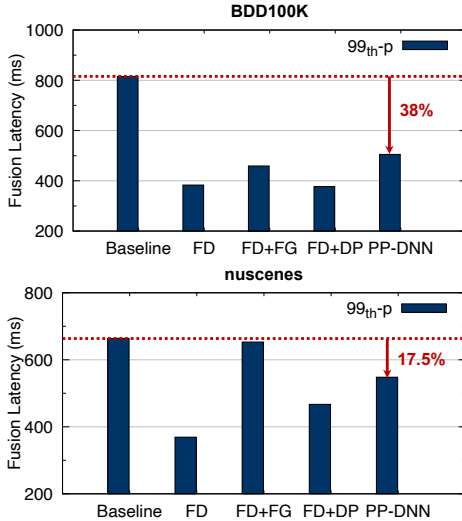


Fig. 10. The 99-th percentile fusion delay.

TABLE V  
THE AVERAGE DELAY FOR TASKS ON BDD100K.

Average Delay (ms)	Faster R-CNN	DNLNet	Deeplabv3+	Fusion	Speedup
Baseline	257.4	311.2	366.2	1988.8	-
FD	261.4	302.7	353.4	434.2	4.6×
FD+FG	261.4	247.1	356.9	570.9	3.5×
FD+DP	<b>249.7</b>	296.6	<b>348.8</b>	<b>275.9</b>	<b>7.2×</b>
PP-DNN	251	<b>226.6</b>	358.1	349.1	5.7×

TABLE VI  
THE AVERAGE DELAY FOR TASKS ON NUSCENES.

Delay (ms)	Faster R-CNN	DNLNet	Deeplabv3+	Fusion	Speedup
Baseline	267.7	308.9	367.9	1627.6	-
FD	247.8	309.5	362.2	838.5	1.9×
FD+FG	<b>238.8</b>	216.4	350.6	888.3	1.8×
FD+DP	262.3	308.1	357.5	<b>610.5</b>	<b>2.7×</b>
PP-DNN	250.3	<b>205.2</b>	<b>342.4</b>	632.0	2.6×

### C. Detection Completeness

PP-DNN leverages the ROIs generator to guarantee the detection’s performance on accuracy. We propose a detection completeness metric to evaluate the streaming detection performance when only a group of frames is selected for processing. We first discuss the effectiveness of the detection completeness metric and then present the results of detection completeness for all testing cases.

We collected the message sequence numbers for all five testing cases and compared them with the offline detection results. Also, We collected the detection results for all three tasks when running offline as the ground truth. When PP-DNN is running online, we collected detection results and calculated detection completeness based on Algorithm 2 for each case. The results for the CDF of detection completeness ( $d_c$ ) for all testing cases are shown in Fig. 11. For both BDD100K and nuScenes dataset, we can observe PP-DNN improves object detection completeness and maintains the same level

of detection completeness for lane detection and semantic segmentation. The improvement mainly comes from our implementation of an object tracker for updating the bounding boxes of tracked objects. Table VII includes the average detection completeness for all the testing cases on BDD100K dataset. PP-DNN is found to improve the detection completeness by 186% (from 0.147 to 0.422). This improvement is mainly achieved by FD which skips out-of-date frames. Table VIII includes the average detection completeness for all the testing cases on the nuScenes dataset. PP-DNN is found to improve the detection completeness by 75.4% (from 0.275 to 0.483). It also improves the detection completeness for segmentation by 19.9% (from 0.488 to 0.585). We can observe that the frame ROI generator (FG) enhances the detection completeness using its modeling and process of critical areas. Overall, the detection completeness is enhanced thanks to the frame dispatcher (FD) which skips out-of-date frames and the frame ROI generator (FG) which captures critical areas for detection accuracy.

TABLE VII  
THE DETECTION COMPLETENESS ON BDD100K.

Average Detection Completeness	Faster R-CNN		DNLNet		Deeplabv3+	
	$d_c$	% Change	$d_c$	% Change	$d_c$	% Change
Baseline	0.147	-	0.643	-	0.339	-
FD	<b>0.558</b>	+279%	0.679	+5.6%	0.393	+15.9%
FD+FG	0.437	+196%	<b>0.705</b>	+9.5%	0.380	+12.1%
FD+DP	0.477	+224%	0.691	+7.4%	0.369	+9.1%
PP-DNN	0.422	+186%	0.703	+9.3%	<b>0.399</b>	<b>17.7%</b>

TABLE VIII  
THE DETECTION COMPLETENESS ON NUSCENES.

Detection Completeness	Faster R-CNN		DNLNet		Deeplabv3+	
	$d_c$	% Change	$d_c$	% Change	$d_c$	% Change
Baseline	0.275	-	0.842	-	0.488	-
FD	0.469	+70.2%	<b>0.902</b>	+7.1%	<b>0.593</b>	+21.4%
FD+FG	<b>0.480</b>	+74.2%	0.893	+6.0%	0.583	+19.4%
FD+DP	0.479	+73.9%	0.898	+6.6%	0.582	+19.2%
PP-DNN	0.483	+75.4%	0.877	+4.2%	0.585	+19.9%

### D. Cost-Effectiveness

Fig. 12 shows how effectively PP-DNN enhances both latency and accuracy. In particular, this figure details PP-DNN’s cost-effectiveness using various configurations across the BDD100K and nuScenes datasets, involving the Frame ROI Generator (FG), Frame Dispatcher (FD), and Detection Predictor (DP).

For the BDD100K dataset, by integrating FG, FD, and DP, PP-DNN boosts its cost-effectiveness, showcasing a 98% (from 61.2 to 1.1) improvement over the baseline. This underscores the combined strategy’s role in striking a balance between latency and accuracy. For the nuScenes dataset, PP-DNN demonstrates a notable performance advantage with an 86% (from 14.6 to 2.0) enhancement of cost-effectiveness.

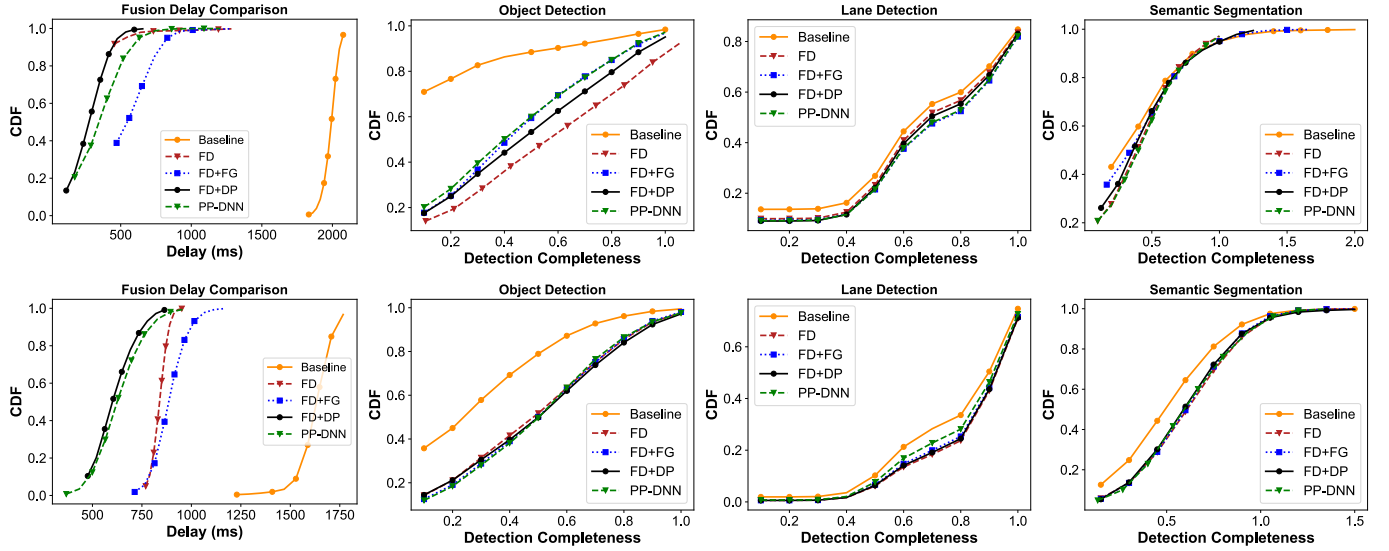


Fig. 11. The CDF of fusion delay and the detection completeness on BDD100K (upper figures) and nuScenes datasets (lower figures).

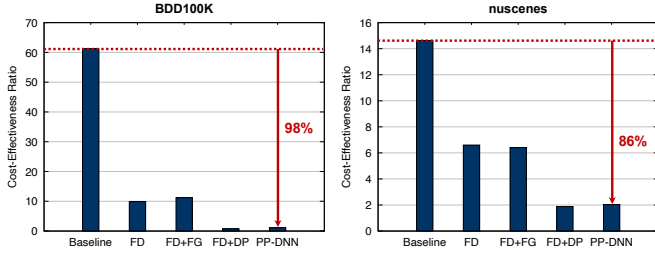


Fig. 12. The 50-th percentile cost-effectiveness.

FD contributes to this increase in cost-effectiveness by skipping outdated frames and facilitating coordinated multi-tenant DNN inference. The integration of FG also improves this metric by selecting critical frames, thereby enhancing detection accuracy without processing every frame. Additionally, DP introduces predictions for non-critical frames, improving the system's efficiency in handling fusion latency. These results suggest that while FG, FD, and DP each play a significant role in enhancing performance, their collective implementation within PP-DNN leads to the most substantial improvements in cost-effectiveness on both datasets.

## VII. RELATED WORK

**Real-time DNN Inference.** Extensive work has been done on real-time DNN inference. One direction of this work was to make the DNN models lightweight. Han *et al.* [12] proposed the pruning of redundant connections to reduce computation demand. Reducing the precision of operations and operands is another direction for the runtime optimization of DNN inference [13], [47]. However, this usually incurs a non-negligible loss of accuracy, which is unacceptable for AVs. The third direction of work is runtime system acceleration and scheduling of the execution pipeline. DeepCache [14]

leverages the temporal locality in streaming video to accelerate the vision tasks on mobile devices. ALERT [15] addresses this with the anytime DNN system, which has multiple outputs at different times. Liu *et al.* [16] proposed a self-cueing attention mechanism that processes critical regions in real time. However, none of them can support real-time multi-tenant DNN inference for AV perception. Prophet [17] provides temporal predictability for multi-tenant DNNs without considering functional predictability. PP-DNN is the first to address both aspects of predictability with multi-tenant DNN inference for AV perception.

**Selection of Video Keyframes.** Video keyframe detection is commonly used in video detection. Xiong *et al.* [48] proposed a learning-based approach to highlight detection with a preference for short videos. Yan *et al.* [49] proposed a deep two-stream ConvNet for keyframe detection in human action videos. Other approaches take multiple input sources for keyframe detection: [50] takes language as additional input while [51] takes audio as additional input. However, all these target scenarios where the video is provided and the detection is done offline [52]. In contrast, detecting keyframes for AV perception is more challenging since whether a frame is a keyframe or not should be decided in real-time, and only information about the past frames is available.

## VIII. CONCLUSION

Predictability of perception latency and accuracy is essential for AV safety. The use of multi-tenant DNNs in the AV perception pipeline imposes high computational demands, making it even more challenging to guarantee both temporally and functionally predictability. We have addressed the predictability of AV perception with a novel approach by reducing the number of image frames to be processed without losing accuracy by dynamically adjusting critical frames and ROIs. We have proposed PP-DNN to trade the number of processed frames

for better predictability and detection with temporal locality. Our in-depth evaluation of the BDD100K dataset and the nuScenes dataset has shown PP-DNN to improve the number of fused frames by  $7.3\times$ , reduce the fusion delay by more than  $2.6\times$  and fusion-delay variations by more than  $2.3\times$ , improve detection completeness by 75.4%, and achieve up to 98% cost-effectiveness improvement over the baseline with acceptable memory overhead.

## REFERENCES

- [1] E. Yurtsever, J. Lambert, A. Carballo, and K. Takeda, “A survey of autonomous driving: Common practices and emerging technologies,” *IEEE access*, vol. 8, pp. 58443–58469, 2020.
- [2] S. Kato, E. Takeuchi, Y. Ishiguro, Y. Ninomiya, K. Takeda, and T. Hamada, “An open approach to autonomous vehicles,” *IEEE Micro*, vol. 35, no. 6, pp. 60–68, 2015.
- [3] J. Redmon and A. Farhadi, “YOLOv3: An incremental improvement,” *arXiv preprint arXiv:1804.02767*, 2018.
- [4] W. Liu, D. Anguelov, D. Erhan, C. Szegedy, S. Reed, C.-Y. Fu, and A. C. Berg, “SSD: Single shot multibox detector,” in *European conference on computer vision*. Springer, 2016, pp. 21–37.
- [5] S. Ren, K. He, R. Girshick, and J. Sun, “Faster R-CNN: Towards real-time object detection with region proposal networks,” in *Advances in neural information processing systems*, 2015, pp. 91–99.
- [6] A. G. Howard, M. Zhu, B. Chen, D. Kalenichenko, W. Wang, T. Weyand, M. Andreetto, and H. Adam, “MobileNets: efficient convolutional neural networks for mobile vision applications,” *arXiv preprint arXiv:1704.04861*, 2017.
- [7] L.-C. Chen, Y. Zhu, G. Papandreou, F. Schroff, and H. Adam, “Encoder-decoder with atrous separable convolution for semantic image segmentation,” in *Proceedings of the European conference on computer vision (ECCV)*, 2018, pp. 801–818.
- [8] D. Neven, B. De Brabandere, S. Georgoulis, M. Proesmans, and L. Van Gool, “Towards end-to-end lane detection: an instance segmentation approach,” in *2018 IEEE intelligent vehicles symposium (IV)*. IEEE, 2018, pp. 286–291.
- [9] S.-C. Lin, Y. Zhang, C.-H. Hsu, M. Skach, M. E. Haque, L. Tang, and J. Mars, “The architectural implications of autonomous driving: Constraints and acceleration,” in *Proceedings of the Twenty-Third International Conference on Architectural Support for Programming Languages and Operating Systems*. ACM, 2018, pp. 751–766.
- [10] I. Gog, S. Kalra, P. Schafhalter, J. E. Gonzalez, and I. Stoica, “D3: a dynamic deadline-driven approach for building autonomous vehicles,” in *Proceedings of the Seventeenth European Conference on Computer Systems*, 2022, pp. 453–471.
- [11] L. Liu, S. Lu, R. Zhong, B. Wu, Y. Yao, Q. Zhang, and W. Shi, “Computing systems for autonomous driving: State of the art and challenges,” *IEEE Internet of Things Journal*, vol. 8, no. 8, pp. 6469–6486, 2020.
- [12] S. Han, J. Pool, J. Tran, and W. J. Dally, “Learning both weights and connections for efficient neural networks,” *arXiv preprint arXiv:1506.02626*, 2015.
- [13] Z. Cai, X. He, J. Sun, and N. Vasconcelos, “Deep learning with low precision by half-wave gaussian quantization,” in *Proceedings of the IEEE Conference on Computer Vision and Pattern Recognition*, 2017, pp. 5918–5926.
- [14] M. Xu, M. Zhu, Y. Liu, F. X. Lin, and X. Liu, “Deepcache: Principled cache for mobile deep vision,” in *Proceedings of the 24th Annual International Conference on Mobile Computing and Networking*, 2018, pp. 129–144.
- [15] C. Wan, M. Santraiji, E. Rogers, H. Hoffmann, M. Maire, and S. Lu, “ALERT: Accurate learning for energy and timeliness,” in *2020 USENIX Annual Technical Conference (USENIX ATC 20)*, 2020, pp. 353–369.
- [16] S. Liu, X. Fu, M. Wigness, P. David, S. Yao, L. Sha, and T. Abdelzaher, “Self-cueing real-time attention scheduling in criticality-aware visual machine perception,” in *2022 IEEE 28th Real-Time and Embedded Technology and Applications Symposium (RTAS)*. IEEE, 2022, pp. 173–186.
- [17] L. Liu, Z. Dong, Y. Wang, and W. Shi, “Prophet: Realizing a predictable real-time perception pipeline for autonomous vehicles,” in *The IEEE Real-Time Systems Symposium (RTSS)*, 2022.
- [18] F. Yu, H. Chen, X. Wang, W. Xian, Y. Chen, F. Liu, V. Madhavan, and T. Darrell, “Bdd100k: A diverse driving dataset for heterogeneous multitask learning,” in *Proceedings of the IEEE/CVF conference on computer vision and pattern recognition*, 2020, pp. 2636–2645.
- [19] H. Caesar, V. Bankiti, A. H. Lang, S. Vora, V. E. Liog, Q. Xu, A. Krishnan, Y. Pan, G. Baldan, and O. Beijbom, “nuscenes: A multimodal dataset for autonomous driving,” in *Proceedings of the IEEE/CVF conference on computer vision and pattern recognition*, 2020, pp. 11621–11631.
- [20] R. Mur-Artal and J. D. Tardós, “ORB-SLAM2: An open-source slam system for monocular, stereo, and rgb-d cameras,” *IEEE transactions on robotics*, vol. 33, no. 5, pp. 1255–1262, 2017.
- [21] K. He, G. Gkioxari, P. Dollár, and R. Girshick, “Mask R-CNN,” in *Proceedings of the IEEE international conference on computer vision*, 2017, pp. 2961–2969.
- [22] Y. Ko, J. Jun, D. Ko, and M. Jeon, “Key points estimation and point instance segmentation approach for lane detection,” *arXiv preprint arXiv:2002.06604*, 2020.
- [23] T. Zheng, H. Fang, Y. Zhang, W. Tang, Z. Yang, H. Liu, and D. Cai, “Resa: Recurrent feature-shift aggregator for lane detection,” *arXiv preprint arXiv:2008.13719*, vol. 5, no. 7, 2020.
- [24] X. Pan, J. Shi, P. Luo, X. Wang, and X. Tang, “Spatial as deep: Spatial CNN for traffic scene understanding,” in *Thirty-Second AAAI Conference on Artificial Intelligence*, 2018.
- [25] O. Ronneberger, P. Fischer, and T. Brox, “U-net: Convolutional networks for biomedical image segmentation,” in *International Conference on Medical image computing and computer-assisted intervention*. Springer, 2015, pp. 234–241.
- [26] F. Hafeez, U. U. Sheikh, N. Alkhaldi, H. Z. Al Garni, Z. A. Arfeen, and S. A. Khalid, “Insights and strategies for an autonomous vehicle with a sensor fusion innovation: a fictional outlook,” *IEEE Access*, vol. 8, pp. 135162–135175, 2020.
- [27] D. Lu, “global\_planner,” [http://wiki.ros.org/global\\_planner](http://wiki.ros.org/global_planner).
- [28] E. Marder-Eppstein, “dwa\_local\_planner,” [http://wiki.ros.org/dwa\\_local\\_planner](http://wiki.ros.org/dwa_local_planner).
- [29] M. Bertoluzzo, P. Bolognesi, O. Bruno, G. Buja, A. Landi, and A. Zuccollo, “Drive-by-wire systems for ground vehicles,” in *2004 IEEE International Symposium on Industrial Electronics*, vol. 1. IEEE, 2004, pp. 711–716.
- [30] Y.-J. Pan, C. Canudas-de Wit, and O. Sename, “A new predictive approach for bilateral teleoperation with applications to drive-by-wire systems,” *IEEE Transactions on Robotics*, vol. 22, no. 6, pp. 1146–1162, 2006.
- [31] M. Farsi, K. Ratcliff, and M. Barbosa, “An overview of controller area network,” *Computing & Control Engineering Journal*, vol. 10, no. 3, pp. 113–120, 1999.
- [32] M. Li, Y.-X. Wang, and D. Ramanan, “Towards streaming perception,” in *Computer Vision–ECCV 2020: 16th European Conference, Glasgow, UK, August 23–28, 2020, Proceedings, Part II 16*. Springer, 2020, pp. 473–488.
- [33] W. Kang, S. Chung, J. Y. Kim, Y. Lee, K. Lee, J. Lee, K. G. Shin, and H. S. Chwa, “Dnn-sam: Split-and-merge dnn execution for real-time object detection,” in *2022 IEEE 28th Real-Time and Embedded Technology and Applications Symposium (RTAS)*. IEEE, 2022, pp. 160–172.
- [34] L. Liu, Y. Wang, and W. Shi, “Understanding time variations of dnn inference in autonomous driving,” *arXiv preprint arXiv:2209.05487*, 2023.
- [35] L.-C. Chen, G. Papandreou, F. Schroff, and H. Adam, “Rethinking atrous convolution for semantic image segmentation,” *arXiv preprint arXiv:1706.05587*, 2017.
- [36] M. Quigley, K. Conley, B. Gerkey, J. Faust, T. Foote, J. Leibs, R. Wheeler, A. Y. Ng *et al.*, “Ros: an open-source robot operating system,” in *ICRA workshop on open source software*, vol. 3, no. 3.2. Kobe, Japan, 2009, p. 5.
- [37] “message\_filters,” [http://wiki.ros.org/message\\_filters](http://wiki.ros.org/message_filters).
- [38] NVIDIA, “CUDA Toolkit Documentation v11.6.0,” <https://docs.nvidia.com/cuda/archive/11.6.0/>.
- [39] A. Clark *et al.*, “Pillow (pil fork) documentation,” *readthedocs*, 2015.
- [40] Z. Wang, A. C. Bovik, H. R. Sheikh, and E. P. Simoncelli, “Image quality assessment: from error visibility to structural similarity,” *IEEE Transactions on Image Processing*, vol. 13, no. 4, pp. 600–612, 2004.
- [41] N. Wojke, A. Bewley, and D. Paulus, “Simple online and realtime tracking with a deep association metric,” in *2017 IEEE International Conference on Image Processing (ICIP)*. IEEE, 2017, pp. 3645–3649.

- [42] N. Wojke and A. Bewley, “Deep cosine metric learning for person re-identification,” in *2018 IEEE Winter Conference on Applications of Computer Vision (WACV)*. IEEE, 2018, pp. 748–756.
- [43] A. Bochkovskiy, C.-Y. Wang, and H.-Y. M. Liao, “YOLOv4: optimal speed and accuracy of object detection,” *arXiv preprint arXiv:2004.10934*, 2020.
- [44] Autoware, “AD Computers,” <https://autowarefoundation.github.io/autoware-documentation/main/reference-hw/ad-computers/>.
- [45] AWS, “EC2 Instances (G5) with NVIDIA A10G Tensor Core GPUs,” <https://aws.amazon.com/blogs/aws/new-ec2-instances-g5-with-nvidia-a10g-tensor-core-gpus/>.
- [46] M. Yin, Z. Yao, Y. Cao, X. Li, Z. Zhang, S. Lin, and H. Hu, “Disentangled non-local neural networks,” in *European Conference on Computer Vision*. Springer, 2020, pp. 191–207.
- [47] V. Sze, Y.-H. Chen, T.-J. Yang, and J. S. Emer, “Efficient processing of deep neural networks: A tutorial and survey,” *Proceedings of the IEEE*, vol. 105, no. 12, pp. 2295–2329, 2017.
- [48] B. Xiong, Y. Kalantidis, D. Ghadiyaram, and K. Grauman, “Less is more: Learning highlight detection from video duration,” in *Proceedings of the IEEE/CVF conference on computer vision and pattern recognition*, 2019, pp. 1258–1267.
- [49] X. Yan, S. Z. Gilani, H. Qin, M. Feng, L. Zhang, and A. Mian, “Deep keyframe detection in human action videos,” *arXiv preprint arXiv:1804.10021*, 2018.
- [50] M. Narasimhan, A. Rohrbach, and T. Darrell, “Clip-it! language-guided video summarization,” *Advances in Neural Information Processing Systems*, vol. 34, pp. 13 988–14 000, 2021.
- [51] T. Badamdarj, M. Rochan, Y. Wang, and L. Cheng, “Joint visual and audio learning for video highlight detection,” in *Proceedings of the IEEE/CVF International Conference on Computer Vision*, 2021, pp. 8127–8137.
- [52] ——, “Contrastive learning for unsupervised video highlight detection,” in *Proceedings of the IEEE/CVF Conference on Computer Vision and Pattern Recognition*, 2022, pp. 14 042–14 052.